Aharonov-Bohm oscillations and magnetic focusing in ballistic graphene rings

Jan Dauber,[1,2] Martin Oellers,[1] Florian Venn,[3] Alexander Epping,[1,2] Kenji Watanabe,[4] Takashi Taniguchi,[4] Fabian Hassler,[3] and Christoph Stampfer[1,2,*]

[1]*JARA-FIT and 2nd Institute of Physics, RWTH Aachen University, 52074 Aachen, Germany*
[2]*Peter Grünberg Institute (PGI-9), Forschungszentrum Jülich, 52425 Jülich, Germany*
[3]*JARA Institute for Quantum Information at RWTH Aachen University, Aachen, Germany*
[4]*National Institute for Materials Science, 1-1 Namiki, Tsukuba, Japan*

We present low-temperature magnetotransport measurements on graphene rings encapsulated in hexagonal boron nitride. We investigate phase-coherent transport and show Aharonov-Bohm (AB) oscillations in quasiballistic graphene rings with hard confinement. In particular, we report on the observation of h/e, $h/2e$, and $h/3e$ conductance oscillations. Moreover we show signatures of magnetic focusing effects at small magnetic fields confirming ballistic transport. We perform tight-binding calculations which allow us to reproduce all significant features of our experimental findings and enable a deeper understanding of the underlying physics. Finally, we report on the observation of the AB conductance oscillations in the quantum Hall regime at reasonable high magnetic fields, where we find regions with enhanced AB oscillation visibility with values up to 0.7%. These oscillations are well explained by taking disorder into account allowing for a coexistence of hard- and soft-wall confinement.

I. INTRODUCTION

Quantum interference and ballistic transport are corner stones of mesoscopic physics [1] giving rise to many interesting effects, such as weak localization corrections, universal conductance fluctuations [2], quantized conductance [3], persistent currents [4], Aharonov-Bohm oscillations [5], and many others. These effects are known to depend strongly on system size and characteristic length scales of electron transport, such as the elastic mean-free path and the phase-coherence length. As these length scales are crucially affected by impurity and defect scattering as well as by electron-phonon and electron-electron interactions; high-purity materials and low temperatures are vital for controlling and utilizing quantum interference phenomena in mesoscopic systems. For experimentally addressing these phenomena two-dimensional (2D) electron systems based on III-V heterostructures have proven to be a very favorable platform.

Thanks to the recent advances in process technologies of assembling 2D materials [6], we nowadays have micrometer-sized graphene samples with elastic mean-free paths exceeding values of 25 μm [7]. These advances not only start closing the gap between graphene and the most favorable GaAs-based 2D electron systems but they also open the door to Dirac-fermion-based mesoscopic devices with a hard-wall confinement and to a unique platform for electron optics [8,9]. Recently a number of interesting devices and phenomena based on ballistic transport in graphene have been demonstrated, ranging from Fabry-Perot and commensurability oscillations [10,11] to magnetic focusing [12] and the Veselago lens [13] to Klein tunneling transistors [14], and even ballistic graphene Josephson junctions [15]. All these devices rely on high-mobility graphene with large lateral dimensions such that edges are not limiting transport.

In this work we show that ballistic transport in state-of-the-art graphene can also be maintained when carving out mesoscopic rings, allowing us to study electron interference in mesoscopic devices with a truly hard-wall confinement and a widely tunable Fermi wavelength. In particular we present low-temperature magnetotransport measurements on graphene rings exhibiting ballistic transport, Aharonov-Bohm conductance oscillations, and magnetic focusing. Aharonov-Bohm (AB) interference [16] experiments on ring structures have been proven to be useful for observing and controlling interference patterns as they provide a straightforward way for shifting the phase by a small out-of-plane magnetic field. The AB effect has been studied in detail in rings based on metallic films [5], on semiconductor heterostructures [17], and more recently also on graphene [18–25]. Here it is important to note that in all previous studies on graphene rings, the samples have been in the diffusive regime, which in contrast to ballistic transport (i) leads to a strong suppression of AB oscillations at very low carrier densities [18], (ii) does not allow us to access magnetic focusing, and (iii) prohibits the probing of the coexistence of hard- and soft-wall confinement.

As graphene only consists of surface atoms, the sample quality is highly influenced by disorder arising from substrate interaction and edge roughness [26,27]. By fully encapsulating graphene in hexagonal boron nitride (hBN) the sample quality is improved substantially [28–31]. Importantly, this improvement also holds for hBN-graphene-hBN structures with lateral dimensions down to around 200 nm [32]. For smaller structures disorder due to the rough edges of graphene leading to localized states strongly limits high-mobility transport [32–34]. Our work is based on this recent insights and we report (i) on the fabrication of graphene rings fully encapsulated in hBN, (ii) on phase-coherent transport with a focus on AB oscillations for small magnetic fields, and (iii) on the observation of electron guiding and magnetic focusing for intermediate magnetic fields indicating quasiballistic transport. Moreover, we perform tight-binding calculations of graphene rings with

---

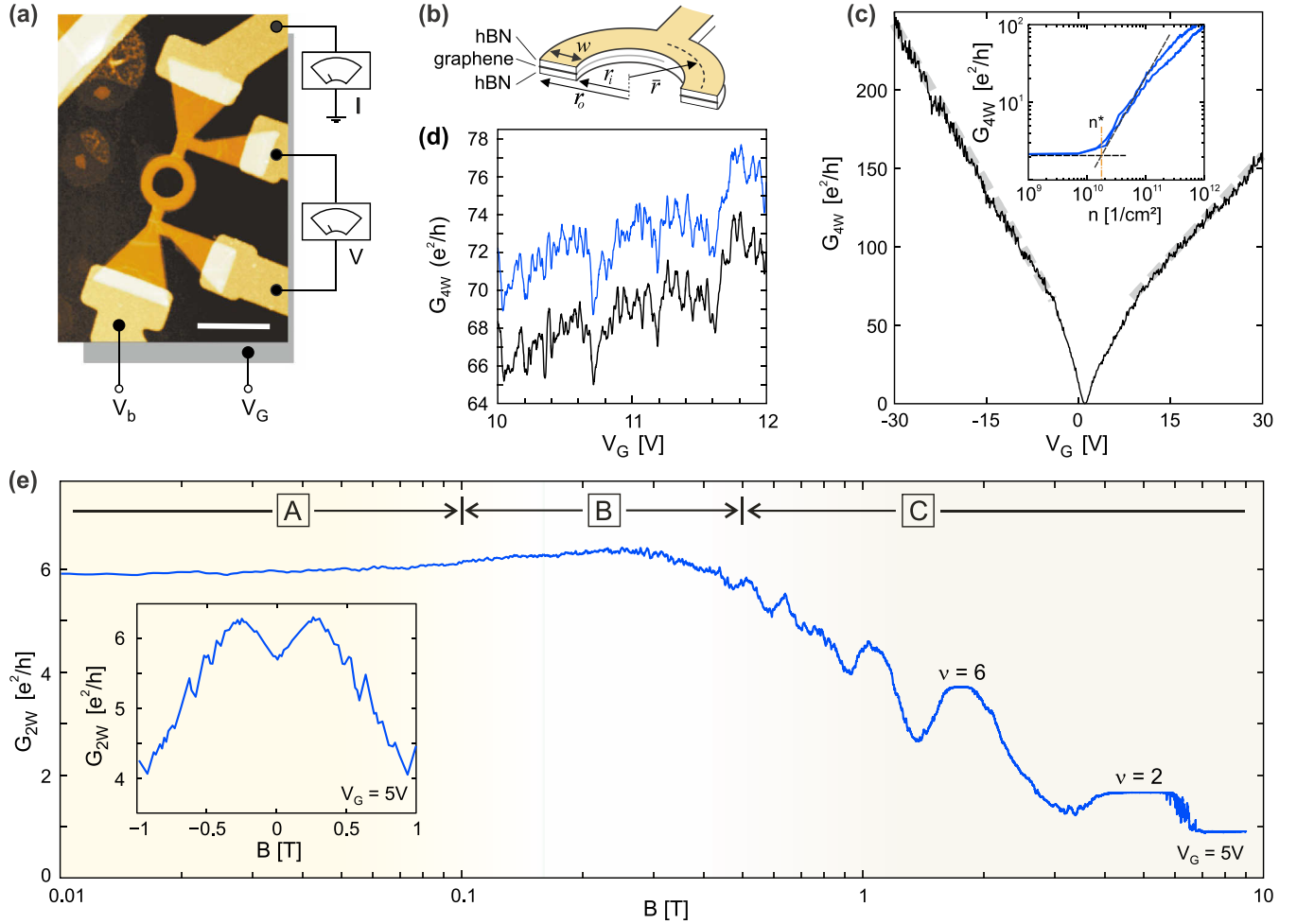*Corresponding author: stampfer@physik.rwth-aachen.de

FIG. 1. (a) Scanning force microscopy image of device 1 with a schematic of the measurement configuration. The white scale bar is 2 μm. (b) Illustration highlighting the cross section of the ring device and its dimensions (see text). (c) G_{4W} as a function of V_G at $B = 0$ T. Dashed lines represent fits for extracting the field effect mobility μ. Inset shows log-log plot for the extraction of n^*. (d) Repeated measurements of G_{4W} over a smaller range of V_G showing universal conductance fluctuations with good reproducibility. The traces are offset by $4e^2/h$ for clarity. (e) G_{2W} as a function of B at $V_G = 5$ V. The B-field axis is divided into three regimes: low-field ($r_C > w$; label A), intermediate-field ($r_C \approx w$; label B), and high-field range ($r_C < w/2$; label C). The inset shows G_{2W} for $|B| \leqslant 1$ T. All measurements are taken at $T = 36$ mK.

similar geometries and compare the simulation results with the measurements, being able to assign specific skipping orbits to signatures in the measured conductance traces. Finally, we discuss highly visible AB oscillations at the onset of well-established quantum Hall plateaus in experiment and theory.

II. METHODS

We present measurements on two samples with different geometry. Unless stated otherwise data from sample 1 are shown. The samples have been fabricated by stacking mechanically exfoliated graphene and hBN with the dry-transfer technique based on van der Waals adhesion introduced by Wang *et al.* [31] on highly p-doped Si substrates with a 285 nm thick SiO$_2$ top layer. The hBN-graphene-hBN sandwiches have been structured by reactive ion etching (SF$_6$/Ar plasma) using an AZ nLOF 2020 mask patterned by electron beam lithography (EBL). Electrical contacts to the etched devices have been made by a second EBL step, metal evaporation (5 nm Cr/95 nm

Au) and standard liftoff process. A scanning force microscopy (SFM) image of the final device 1 is shown in Fig. 1(a). From the SFM image we extract an inner and an outer ring radius of $r_i = 405$ nm and $r_o = 755$ nm, respectively [see also Fig. 1(b)]. These numbers results in a mean radius of $\bar{r} = 580$ nm and a width of the ring arms of $w = r_o - r_i = 350$ nm. The second sample has slightly different dimensions exhibiting a mean radius of $\bar{r} = 500$ nm and a width of the ring arms of $w = 200$ nm. All measurements are performed in a dilution refrigerator with base temperature of around $T = 36$ mK and perpendicular magnetic field up to 9 T using standard low-frequency lock-in techniques for simultaneous two (2W) and four-terminal (4W) measurements. The two-terminal current is measured with a home-built I/V converter and a low-noise amplifier in combination with a standard lock-in amplifier, whereas the four-terminal voltage drop is measured directly by the lock-in as illustrated in Fig. 1(a). For the data analysis of the magnetic-field-dependent measurement we mainly concentrate on the two-terminal measurements, as the data quality is better thanks to preamplification.

The quantum transport simulation has been performed using a tight-binding approximation on a hexagonal lattice with the Kwant package [35]. We have simulated a scaled version of the graphene lattice with a lattice constant that is a factor 10 larger than the experimental situation and our simulation involves in total 7×10^5 lattice sites. All results are presented in original units for easier comparison to the experimental findings. For more details on the simulation methodology, see the Appendix.

III. RESULTS AND DISCUSSION

Figure 1(c) shows the four-terminal back-gate characteristics for zero magnetic field at base temperature. At high gate voltage V_G we observe a linear dependence of the four-terminal conductance G_{4W} as a function of V_G with a slope of $\Delta G_{4W}/\Delta V_G$ (see dashed lines). We conservatively estimate the square conductance $G_\square = en\mu \approx 4G_{4W}$ from the sample geometry [36]. As the charge carrier density n is directly linked to V_G by $n = \alpha(V_G - V_{CNP})$, we find the field effect mobility by $\mu \approx 1/(4e\alpha)(\Delta G_{4W}/\Delta V_G)$. Here, $\alpha = 6.7 \times 10^{10}$ cm^{-2} V^{-1} is the gate lever arm, which has been extracted from quantum Hall measurements (see below), e is the elementary charge, and the charge neutrality point (CNP) is around $V_{CNP} \approx 1$ V. We obtain field effect mobilities of $\mu_h \approx 100\,000$ cm^2 V^{-1} s^{-1} for hole and $\mu_e \approx 60\,000$ cm^2 V^{-1} s^{-1} for electron transport. These mobility values correspond to a mean-free path in the range of $l_m \approx 400$ nm to 1.6 μm (for $V_G = 10$–30 V) [37] highlighting that the transport can be considered as quasiballistic ($w < l_m < l$, where l is the sample length exceeding $\pi\bar{r}$) and that the approximate diffusive description only holds due to boundary scattering at the device edges. With the Einstein relation we estimate the diffusion constant $D = n\,\mu/(e\rho)$, where ρ is the density of states of graphene. By following Ref. [18] we express ρ as function of n and obtain $\rho = 4/(hv_F)\sqrt{\pi n}$, where $v_F = 10^6$ m/s is the Fermi velocity and h the Planck constant. For electron transport we thus extract a diffusion constant of $D = 0.28$–0.49 m^2/s (for $V_G = 10$–30 V). These values are close to the value of the diffusion constant only taking into account scattering at the edges of the narrow leads and the ring arms ($D = wv_F = 0.35$ m^2/s). The high sample quality is moreover reflected in the low residual charge carrier density n^* found to be on the order of 2×10^{10} cm^{-2}, extracted as shown in the inset of Fig. 1(c) [38]. By having a closer look at the four-terminal back-gate characteristics we observe well reproducible universal conductance fluctuations (UCFs) with an amplitude of up to $2e^2/h$ [see Fig. 1(d), a close-up of Fig. 1(c)]. The UCFs are strong evidence for phase-coherent transport.

In Fig. 1(e) the two-terminal conductance G_{2W} is plotted as a function of magnetic field B at $V_G = 5$ V in the near vicinity of the CNP. For small magnetic fields we observe a nearly linear increase of G_{2W} as a function of B [see inset in Fig. 1(e)] with G_{2W} reaching a maximum at $B = \pm 0.3$ T. At higher B fields we observe signatures originating from the quantum Hall effect. As the two-terminal conductance G_{2W} contains contributions from the longitudinal G_{xx} and the Hall conductance G_{xy} we observe dips before entering quantum Hall plateaus, which are typical for two-terminal devices,

where the sample length l is larger than the width w (sample 1 $w = 350$ nm to $l \sim$ several μm) [39]. Quantum Hall plateaus are quite visible for filling factors $\nu = 2$ and 6 [see labels in Fig. 1(d)]. The difference in conductance with respect to the theoretically expected plateaus at $2e^2/h$ and $6e^2/h$ is due to additional resistances from the setup and the contact resistance of the graphene-metal interface included in the two-terminal measurement. With the known setup resistance $R_S \approx 2.3$ kΩ, we estimate an overall contact resistance of $R_C \approx 200$ Ω for each contact.

To systematically discuss the magnetic-field-dependent conductance measurements we divide the B-field range into three regimes based on the ratios of the width of the ring arms w (as well as the mean ring radius $\bar{r}$) and the cyclotron radius $r_C = \hbar\sqrt{\pi n}/eB$ (here $\hbar$ is the reduced Planck constant). First (Sec. III A) we focus on small B fields such that $w, \bar{r} \ll r_C$. In this regime [see label A in Fig. 1(e)] we mainly concentrate on AB oscillations and their dependence on charge carrier density. Second (Sec. III B) we discuss magnetic focusing and localization effects in the regime, where the cyclotron radius is on the order of w and $\bar{r}$ (i.e., $w, \bar{r} \sim r_C$); see label B in Fig. 1(e). Third (Sec. III C) we focus on quantum interference phenomena in the quantum Hall regime (label C), where r_C is significantly smaller than w and $\bar{r}$. In particular, we require $r_C < w/2$ for entering the regime of quantum Hall edge transport.

A. Aharonov-Bohm oscillations at low B fields

Figure 2(a) shows the two-terminal conductance G_{2W} as a function of magnetic field in the small magnetic field range $|B| \leqslant 50$ mT at $V_G = 3$ V. In this regime we observe the presence of AB oscillations as well as UCFs and an overall increase of the conductance with absolute value of magnetic field. As the change of conductance due to AB interference is on the order of a few percent and overlapping with UCFs, additional data postprocessing is needed to extract the periodicity ΔB_{AB} and the amplitude of the AB oscillations ΔG_{AB}. We apply a moving average over a window of $\Delta B = 15$ mT, which is sufficiently larger than the expected periodicity $\Delta B_{AB} = 2.3$–8 mT for the h/e mode [40], and subtract the averaged data from the raw signal [see red dashed line in Fig. 2(a)]. Figure 2(b) displays the processed data of the two-terminal conductance $\Delta G_{2W} = G_{2W} - \langle G_{2W}\rangle_{\Delta B}$ versus magnetic field B. In this plot horizontal lines with a spacing of $\Delta B_{AB} = 5.2$ mT indicate the expected periodicity of the AB oscillations for an ideal ring device with a radius of 580 nm, which corresponds to the mean radius of our fabricated graphene ring. In general, the conductance oscillations are found to be mainly equidistant, but also additional modulations and local derivations are observed. Figure 2(c) depicts similar data, but for different gate voltages (see labels). Interestingly, for higher gate voltages the AB amplitude decreases, while the periodicity is preserved. This observation is summarized in Fig. 2(d), where ΔG_{AB} is plotted as a function of V_G. Here ΔG_{AB} is defined as the root-mean-square amplitude of ΔG_{2W}. Strikingly, the maximum visibility [41] is found close to the charge neutrality point at $V_G = 3$ V and is around 0.25% with respect to the overall conductance G_{2W}. Although the maximum two-terminal visibility is similar to earlier experi-
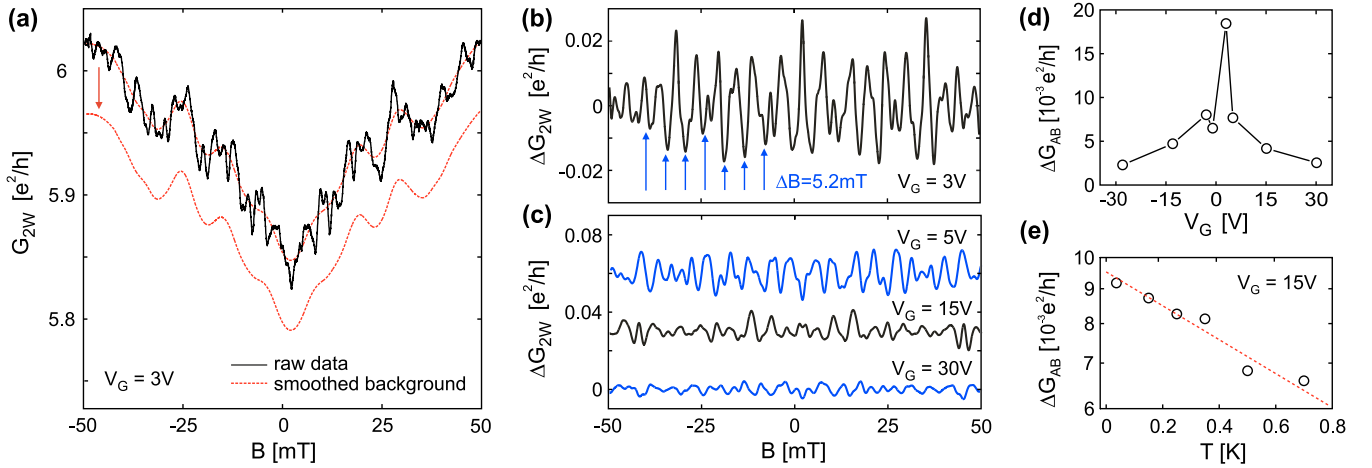
FIG. 2. (a) Solid black line: G_{2W} as a function of B at $V_G = 3$ V. Red dashed lines shows $\langle G_{2W} \rangle$ used for background subtraction. For clarity the trace is duplicated with an offset (see red arrow). (b) and (c) Processed data with ΔG_{2W} for various V_G. Vertical arrows in panel (b) indicate a periodicity of $\Delta B_{AB} = 5.2$ mT. In panel (c) the traces are plotted with an offset for clarity. (d) ΔG_{AB} as a function of V_G. All these measurements are taken at $T = 36$ mK. (e) ΔG_{AB} as a function of T at $V_G = 15$ V. Red dashed line represents an exponential fit to the data $\Delta G_{AB} \propto \exp(-T/T_0)$ with $T_0 = 1.75$ K.

ments on diffusive graphene rings [18,22], the carrier density dependency is inverted. For example, in contrast to Ref. [18] we observe a decreasing amplitude ΔG_{AB} for increasing gate voltage V_G. We explain this behavior by an increasing asymmetric transmission through the two ring arms coming along with an increasing mean-free path l_m as a function of carrier density. Entering the quasiballistic transport regime, the transmission through each of the two arms depends on the specific microscopic sample shape and disorder potentials. Therefore, the transmission is not symmetric, leading to a reduced visibility of AB oscillation [42]. Also with increasing charge carrier density the Fermi wavelength $\lambda_F = \sqrt{4\pi/n}$ is decreasing allowing a higher number of wave modes inside the ring, which may also decrease ΔG_{AB} as it is observed in semiconductor heterostructures [43].

In Fig. 2(e), ΔG_{AB} is plotted as a function of temperature T at $V_G = 15$ V. The decrease of the amplitude ΔG_{AB} with an increase of T follows an overall $\Delta G_{AB} \propto \exp(-T)$ dependence. Due to thermal averaging of the h/e oscillations and changes in the phase-coherence length l_ϕ, the AB amplitude decays as $\Delta G_{AB} \propto (E_{Th}/k_B T)^{1/2} \exp(-\pi \overline{r}/l_\phi)$, where E_{Th} is the Thouless energy and k_B the Boltzmann constant [18]. In a diffusive system, E_{Th} is given by $E_{Th} = \hbar D/L^2$ with characteristic length scale L. Using the diffusion constant determined above $D = 0.36$ m^2/s (for $V_G = 15$ V) and $L = \pi \overline{r}$, we estimate $E_{Th} = 71$ μeV, which corresponds to a critical temperature of $T_c = E_{Th}/k_B = 830$ mK. Without thermal averaging the phase-coherence length is primarily limited by electron-electron scattering following a temperature dependence given by $l_\phi \propto T^{-1}$ as also reported for ballistic one-channel rings in GaAs heterostructures [44]. Thus, a decay $\propto \exp(-T)$ of the AB amplitude is expected below T_c which is in reasonable agreement with our observation in Fig. 2(e). Due to a limited accessible temperature range we cannot extract T_c from the data and determine the energy scale, when thermal averaging contributes to decoherence of AB oscillations.

For further analyzing the AB oscillations we preform fast Fourier transformation (FFT) of the processed data, as shown exemplarily for $V_G = 3$ V in Fig. 3(a). The Fourier spectrum shows a broad band of frequencies that constitute the signal. Peaks for frequencies below the expected AB oscillations, which we attribute to artifacts from the data averaging of a 15 mT moving window (corresponding to 66 1/T) are neglected in the further discussion. The interval of the h/e mode frequencies is given by the sample geometry ranging from 125 to 433 1/T as indicated in Fig. 3(a). The main contribution is around the frequency related to the mean radius $\overline{r}$ of the ring, although features at lower and higher frequencies are present. The broad spread is due to the aspect ratio of mean radius $\overline{r}$ and the width w of the ring, $\overline{r}/w \sim 1.6$. Notably, this circumstance makes any attempt to distinguish contributions from the h/e and $h/2e$ mode difficult as the differences in enclosed area for different paths overlap [see also horizontal arrows in Fig. 3(a)]. This experimental observation is also well reproduced by tight-binding calculations as described above [see Fig. 3(b)]. In the simulations, the AB oscillations exhibit a higher amplitude than in the experiment, which we attribute to the perfectly symmetric transmission through both ring arms and the lack of any other experimental limitations, such as bulk disorder and contact resistance mentioned above. These effects are not included in the calculations since they are not relevant to the investigated physics. The overall behavior of the conduction fluctuations in the wider ring is comparable to the experimental data and the FFT analysis gives similar results [compare black traces in Figs. 3(a) and 3(c)]. Again, a broad range of frequency components is observed in the given ranges of AB mode making a clear assignment of FFT peaks to mode number more than difficult. The narrower ring with a larger aspect ratio ($\overline{r} = 700$ nm, $w = 200$ nm) exhibits a lower amplitude ΔG_{AB} in the calculations, but more distinguishable peaks in the FFT spectrum [compare traces in Fig. 3(c)]. Now peaks only appear close to the center of the corresponding mode ranges and are unambiguously identified
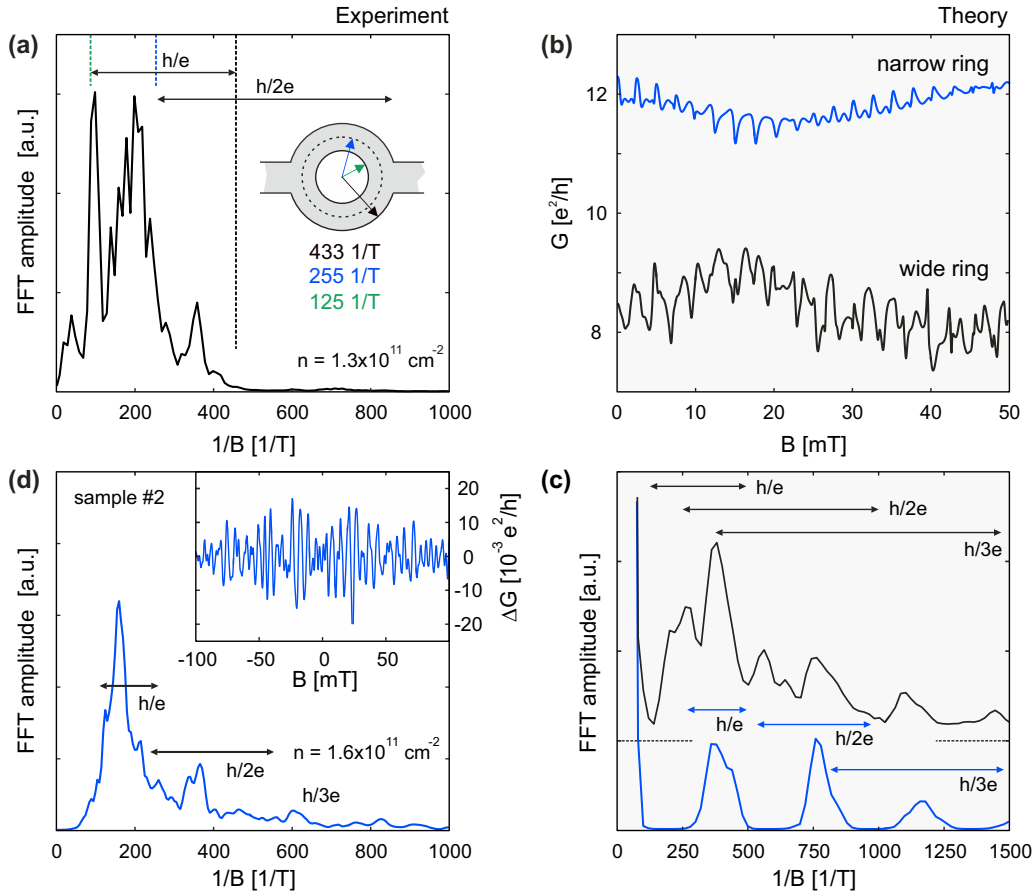
FIG. 3. (a) Fourier spectrum of the AB oscillations measured at $V_G = 3$ V as shown in Fig. 2(b). Frequency range of individual AB oscillation modes marked by arrows. Horizontal lines indicate frequencies for inner, mean, and outer radii as illustrated in the inset. (b) Tight-binding simulations of magnetoconductance of a wide ring ($\bar{r} = 600$ nm, $w = 400$ nm) similar to sample 1 and a narrow ring ($\bar{r} = 700$ nm, $w = 200$ nm) comparable to sample 2 calculated without edge roughness for $n = 1.6 \times 10^{11}$ cm^{-2} (offset by $4e^2/h$). (c) Fourier spectra of the data presented in panel (b) with indicated AB modes. (d) Fourier spectrum of data from sample 2 for similar n as in panel (a). Inset shows background-subtracted ΔG.

as the fundamental mode and its multiples. Since decoherence, i.e., dephasing, is not implemented in the simulation, many higher harmonics are visible. To confirm these results we measured AB oscillations in sample 2 which has a larger aspect ratio $\bar{r}/w \sim 2.5$. Figure 3(d) displays the FFT spectrum of sample 2 at n similar to that of Fig. 3(a). The ranges of h/e and $h/2e$ conduction oscillations only overlap slightly and peaks of the fundamental mode and the first and second harmonic are observed. In particular, the fact of observing contributions from $h/3e$ conductance oscillations [see label in Fig. 3(d)] allows for the conclusion that the phase-coherence length l_ϕ exceeds the value of ≈ 1.5 μm. Hence the difficulties of AB mode identification for sample 1 arise from the ring geometry and do not primarily reflect on the sample quality and the phase-coherence length.

B. Ballistic electron guiding and magnetic focusing

For magnetic fields of up to $B = 0.5$ T ($w \approx r_C$) we observe an increase of the magnetoconductance before a decrease evolves while entering the quantum Hall regime. In Figs. 4(a) and 4(b) this effect is shown for the two samples at similar charge carrier density $n = 1.3 \times 10^{12}$ cm^{-2} but

different geometries, which differ in the type of connection of the ring structure to the source and drain leads and the width of the ring arms. Sample 1 consists of a kind of a T junction comparable to geometries used in previous experiments for graphene rings on silicon dioxide [18–20] while sample 2 is based on a V-shaped connection similar to experiments on III-V heterostructures [45]. The changes in G_{2W} with B are more pronounced in sample 1 with the T junction, while they are hardly visible in sample 2 [see Fig. 4(b)]. The increase in magnetoconductance for sample 1 is caused by an increase of the average mode transmission as a function of B field at the T junction. From a semiclassical point of view this observation is connected to the fact that straight trajectories ($B = 0$ T) are more likely reflected at the T junction than curved ones ($B \neq 0$ T), as illustrated in Fig. 4(a) (see solid and dashed trajectories in the upper right panel). This effect, however, is strongly reduced in sample 2 because there are many open modes available in the lead region very close to the ring, making transport not very sensitive to the average mode transmission as the overall conductance is limited only by the number of modes in the ring arms [compare different colors in the right panels of Fig. 4(a)]. In other words, there are in any case enough trajectory angles available for entering
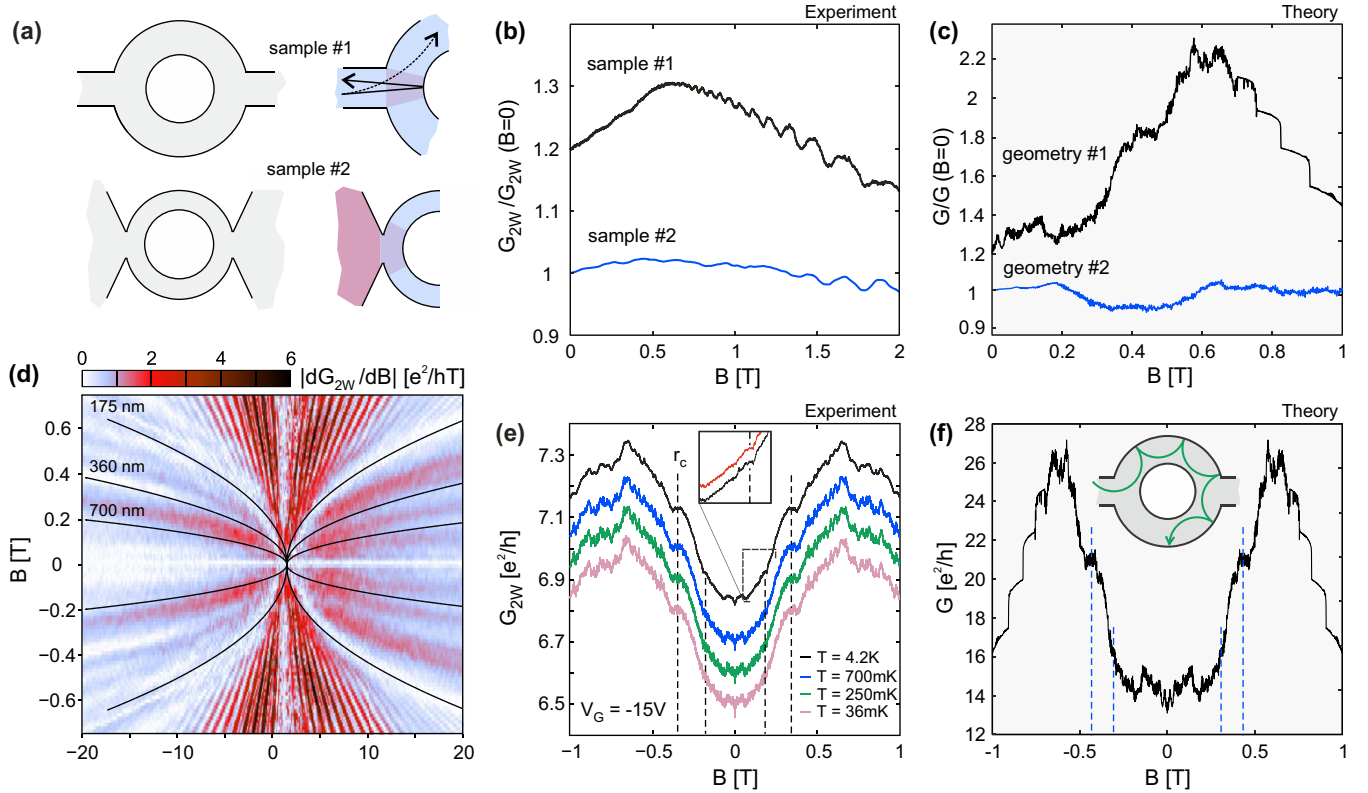
FIG. 4. (a) Schematic representation of the different ring geometries of samples 1 and 2. (b) Magnetoconductance for both samples 1 and 2 in the intermediate magnetic field regime for similar $n \approx 1.3 \times 10^{12}$ cm^{-2} (for sample 1, $V_G = 20$ V). Values are normalized with respect to the conductance at zero B field and an offset is added for clarity. (c) Simulated magnetoconductance G for different device geometries 1 and 2 similar to (b) for $n = 1 \times 10^{12}$ cm^{-2} and $\delta r = 16$ nm (geometry 1: $\bar{r} = 580$ nm, $w = 350$ nm; geometry 2: $\bar{r} = 500$ nm, $w = 200$ nm; plotted with an offset). (d) Derivative of two-terminal conductance with respect to magnetic field dG_{2W}/dB as a function of V_G and B. Solid lines highlight constant cyclotron radii for selected values. (e) Two-terminal conductance G_{2W} versus magnetic field B for $T = 36$ mK and 4.2 K at $V_G = -15$ V ($n = 1 \times 10^{12}$ cm^{-2}). Curves are plotted with offsets for clarity. Vertical dashed lines represent cyclotron radii of $r_C = 360$ and $r_C = 700$ nm. A close up of the 4.2 K trace around $r_C = 360$ is shown as an inset (see also black dashed box). The red trace in the inset corresponds to the (mirrored and vertically offset) negative B-field branch. (f) Conductance G versus magnetic field B of a ring with geometry 1 calculated by tight-binding approach also for $n = 8.5 \times 10^{11}$ cm^{-2} and $\delta r = 16$ nm. Vertical dashed lines again represent cyclotron radii as depicted in panel (d). Inset illustrates the trajectory of charge carriers inside a conductance plateau.

the ring via the V-shaped connection. These observations support the assumption of quasiballistic transport ($w < l_m < l$), because magnetic focusing requires a mean-free path l_m larger than the width w of the ring. In simulations with similar device geometries—geometry 1 (T geometry with $\bar{r} = 580$ nm, $w = 380$ nm) and geometry 2 (V geometry with $\bar{r} = 500$ nm, $w = 200$ nm) and comparable charge carrier density $n = 8.5 \times 10^{11}$ cm^{-2}—we find good qualitative agreement with our experimental findings [see Fig. 4(c)]. The simulations show an increase in magnetoconductance before entering the quantum Hall regime for the T-junction geometry (1) and an almost constant curve for the V-shape geometry (2). Steps indicating the beginning of the quantum Hall effect occur for geometry 1 at $B \approx 0.7$ T, whereas for the narrower geometry 2 they start at $B = 1.2$ T since a smaller cyclotron radius is required (not shown). Intrinsic restrictions of the simulations, such as zero temperature, infinite phase-coherence length, and negligence of contact resistance, lead to additional features. At zero temperature UCFs are enhanced leading to more wobbly traces. Also Shubnikov–de Haas oscillations are not visible due to the absence of thermal broadening of the Landau levels. In

general the simulation results coincide with the experimental observation and the effect is attributed to the interplay of focusing of charge carriers by magnetic field and the type of connection between ring and leads, which is referred to as a size effect. In these measurements we find also plateau-like features in the rising magnetoconductance below $B \leqslant 0.5$ T indicating another size effect related to magnetic field.

Figure 4(d) depicts the derivative of conductance with respect to magnetic field dG_{2W}/dB as a function of V_G and B in a color plot. Here, several features are identified, which show a dependence on the cyclotron radius $r_C(B, V_G) = \hbar\sqrt{\pi\alpha V_G}/(eB)$. As a guide to the eye constant cyclotron radii are drawn in Fig. 4(d) using the gate lever arm α determined from Landau fan measurements (see below). At $r_C = 175$ nm the cyclotron radius matches the requirement for the formation of edge states ($r_C \leqslant w/2$) and we observe the transition to the quantum Hall effect exactly at this limit. In the regime of larger cyclotron radii ($r_C > w/2$) we interestingly observe constant conductance plateaus ($dG_{2W}/dB = 0$) in the B-field-dependent increasing magnetoconductance, which coincide with $r_C \approx 360$ and 700 nm, respectively. For further

investigations G_{4W} versus B is measured at fixed gate voltage $V_G = -15$ V ($n \approx 1 \times 10^{12}$ cm^{-2}) for different temperatures $T = 36$ mK, 250 mK, 700 mK, and 4.2 K [see Fig. 4(e)]. For all temperatures the traces are very similar and only differ in the amplitude of the UCFs and AB oscillations, which almost vanish for 4.2 K. At $B = 350$ mT a conductance plateau is observed, which corresponds to a cyclotron radius of $r_C = 360$ nm. A second conductance plateau is located at $B = 182$ mT (corresponding to $r_C = 700$ nm), but only visible at 4.2 K due to the superposed AB oscillations at lower temperatures. Since the plateaus are observable even in the absence of UCFs and AB oscillations, we conclude that they do not require phase-coherent transport.

The high carrier mobility and the dependency on cyclotron radius indicate that the conductance plateaus are linked to magnetic focusing of charge carriers inside the ring structure [12]. In this case the trajectories of the carriers are deflected by the magnetic field and for some cyclotron radii it becomes more unlikely to exit the ring, which yields in a suppressed increase of magnetoconductance. A schematic illustration of an example of such a trajectory is shown in the inset of Fig. 4(f). For confirming our observation, we carried out tight-binding calculation in the intermediate magnetic field regime. Figure 4(f) shows corresponding simulations for the data shown in Fig. 4(e). Here the conductance plateaus are reproduced quantitatively [compare vertical dashed lines in Figs. 4(e) and 4(f)] by assuming finite edge roughness δr of the graphene ring. The edge roughness introduced by the lithographic pattering of the graphene sheet affects the visibility of the focusing effect and a further analysis of its impact on the simulation results can be found in the Appendix. The smooth steps in the falling edge after the maximum conductance are due to the emerging quantum Hall effect and are not related to magnetic focusing or size quantization effects. Similar observations of magnetic focusing have been made in an AB ring in a GaAs quantum well, where also a T junction has been used and these effects have been attributed to quasiballistic transport with boundary scattering [46]. This type of boundary scattering is quite surprising in consideration of the lithographically etched sample outline and the requirement for specular scattering, that the roughness of the boundaries must be smaller than the Fermi wavelength λ_F [47]. Thus the spatial extension of the disorder potential from the device edge must be smaller than 30 nm, since the focusing feature is still present at gate voltage $|V_G| = 20$ V, which corresponds to $n = 1.4 \times 10^{12}$ 1/cm^2 and $\lambda_F \approx 30$ nm, respectively. In summary, our experimental findings and simulation results point in exactly this direction and strongly support the observation of magnetic focusing in a quasiballistic ring system.

C. High-visibility AB oscillations near quantum Hall plateaus

Next we focus on the high B-field regime ($r_C < w/2$). Figure 5(a) shows a 2D color plot of G_{2W} as a function of V_G and B. We observe a graphene-typical Landau fan for two-terminal measurements with integer Hall plateaus and filling factors up to $\nu = \pm 22$ for $B \leqslant 2$ T. The observation of clear and pronounced features in the Landau fan at such low magnetic fields presupposes a very homogenous doping level, which is also reflected in the low extracted n^*

(see above). Following Ref. [48] we extract the capacitive coupling or so-called lever arm $\alpha = \Delta n / \Delta V_G$ of the back gate from the slope of the Landau levels, which results in $\alpha = 6.7 \times 10^{10}$ cm^{-2} V^{-1} and is in good agreement assuming a parallel plate capacitor model.

In Fig. 5(b) we show several traces of G_{2W} as a function of V_G for various B fields. Quantum Hall signatures are evolving in the vicinity of the CNP below $B = 0.3$ T and are fully developed at $B = 0.5$ T. The dips in magnetoconductance between the conductance plateaus are due to the sample geometry $w < l$ as described above. For $B = 2$ T the conductance plateaus are more pronounced, but also an asymmetry between the hole and electron transport regime becomes apparent, whereas the origin of this remains unclear.

In the B-field range of fully developed quantum Hall plateaus, we find a substantial increase in the visibility of AB oscillations for specific settings of B and V_G [see Fig. 5(c)]. This effect takes place at the flanks, i.e., onsets of quantum Hall plateaus, and is observed only for a few different B-field and gate voltage values. The AB amplitude ΔG_{AB} changes by a factor of 2–3 for small changes in B field on the order of a few tens of milliteslas indicating that they are sensitive to sample inhomogeneities. Figure 5(d) depicts ΔG_{2W} of the data shown in Fig. 5(c). In the best region the AB amplitude reaches a visibility of more than 0.7%, which is a significant increase compared to the low-field regime (≈ 0.25%). This becomes even more apparent in the FFT spectra of the different ranges. Figure 5(e) shows the corresponding FFT spectra and we observe an increase of the FFT amplitude by a factor of three or more. The distinct peaks in the FFT spectra [see, e.g., the blue trace in Fig. 5(e)] moreover show that there are very distinct enclosed areas contributing to the AB oscillations. This is overall in line with edge-channel-dominated transport. Interestingly we find (i) that there is one conductance oscillation frequency [labeled with (1) in Fig. 5(e)] which can be associated with the area enclosed by an edge mode along the inner radius r_i [see vertical dashed line in Fig. 5(e) and red circle in the schematic illustration in Fig. 6(a)] and (ii) that the most pronounced peak in the FFT can be hardly associated and explained with an edge channel traveling along the outer radius r_o (see vertical dashed line). This is on one hand because peak (3) includes area contributions larger than πr_o^2 and on the other hand it is impossible to close such an area by pure edge channel transport. In the regime of fully distinct skipping orbits the edge channels are isolated since the cyclotron radius $r_C < w/2$ prevents inter-edge-channel scattering. The propagating direction inside each edge channel is fixed by the orientation of the perpendicular magnetic field. Hence, individual edge channels fail to enclose an area of magnetic flux and to contribute to AB conductance oscillations by pure edge channel transport. This point is also crucial when considering mechanisms connecting the edge channel propagating along the inner edge of the ring structure [see red circle in Fig. 6(a)].

Consistent with the observation that the conductance oscillations are only present in the crossover regime from one to another filling factor we assume that the disorder potential in the ring entrance or exit region is playing an important role. A present disorder landscape indeed may allow for both (i) accessing the inner edge channel and (ii) connecting the upper
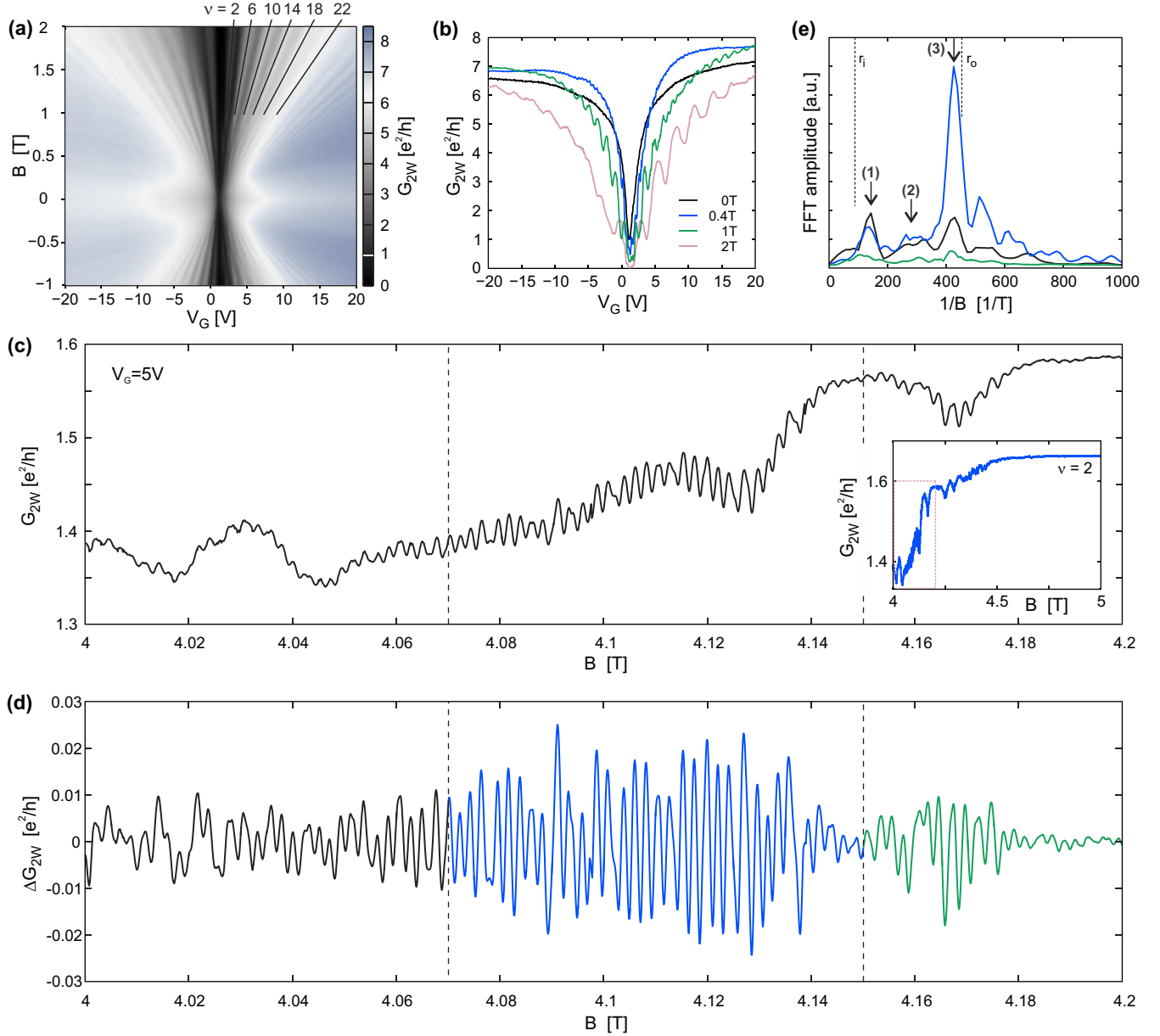
FIG. 5. (a) G_{2W} as a function of V_G and B at $T = 36$ mK. Solid lines represent slopes used for the extraction of α. (b) Line cuts of G_{2W} versus V_G for various B extracted from panel (a). (c) Zoom-in of high-resolution measurements of G_{2W} as a function of B at $V_G = 5$ V in the slope before quantum Hall plateau $\nu = 2$. Inset shows larger measurement range. Red box indicates the selected B-field region. (d) Background-subtracted ΔG_{2W} as a function of B from data shown in panel (c). (e) Fourier spectra of ΔG_{2W} from different regions as depicted in panel (d).

and the lower ring arm [see Fig. 6(a)]. Such a disorder potential is known to arise from substrate interaction, contaminations, or rough edges [49]. It is very likely that in our case there is just one dominating "charge puddle" connecting the two edge states, as scanning tunneling microscopy studies have shown that in graphene on hBN such disorder-induced puddles have typical diameters of around 100–200 nm [50], which is on the order of w.

For a more detailed discussion we performed calculations of magnetotransport through an ideal ring structure (no edge roughness, $\delta r = 0$) with similar dimensions ($w = 400$ nm, $\bar{r} = 600$ nm) and include one charge puddle with a diameter of $d_p = 350$ nm located at the exit region of the ring

[see Fig. 6(a)]. In Fig. 6(b) the calculated local density of states in the quantum Hall regime is plotted for a charge carrier density of $n = 2.8 \times 10^{11}$ cm^{-2} including a charge puddle with an offset in charge carrier density of $\Delta n = -1.6 \times 10^{10}$ cm^{-2} sitting right in the exit region of the ring [see Figs. 6(a) and 6(b)]. Using this charge carrier density for Kwant simulations of magnetotransport the effect of enhanced visibility of AB oscillations is reproduced in a qualitative manner [see Fig. 6(d)], where AB oscillations become most visible between two conductance plateaus (in this example at the step from filling factor 10 to 6). Again, many oscillations are observed with a maximum amplitude in the middle between two quantum Hall plateaus. In Fig. 6(e) we show the
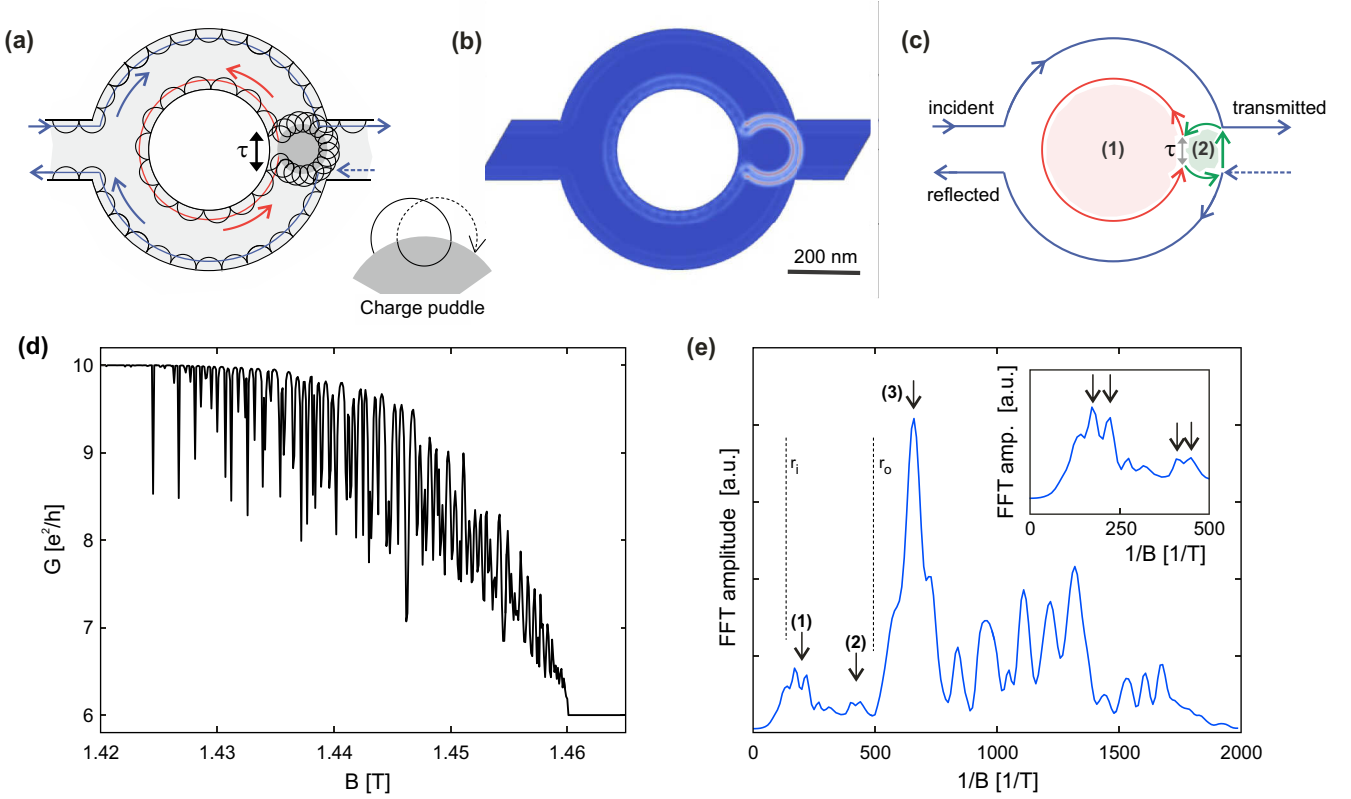
FIG. 6. (a) Schematic illustration of a ring with a charge puddle connecting the inner and outer edge channel in the quantum Hall regime. Arrows indicate the direction of the edge channels. The inset highlights cycloid drift motion of an edge channel along the charge puddle. (b) Calculated density of states of a ring in quantum Hall regime with $n = 2.8 \times 10^{11}$ cm^{-2} and $\delta r = 0$ including a charge puddle with $d_P = 350$ nm and $\Delta n = -1.6 \times 10^{10}$ cm^{-2}. (c) Schematic illustration of the edge states contributing to the interference: the path of the electron that is directly transmitting interferes with the path that encircles the green and red disk (following the arrows). This interference can be tuned via the AB phase of the area (green and red) encircled. Note that in order for interference to happen at all, part of the wave function has to leak to the reflecting edge channel as otherwise unitarity ensures perfect transmission. (d) Calculated conductance G as a function of magnetic field between two quantum Hall plateaus based on the density of states shown in panel (b). (e) Fourier spectrum of background-subtracted calculated conductance. The inset shows a close-up of the FFT spectrum. For more information see text.

corresponding Fourier spectrum of the background-subtracted conductance and the spectrum exhibits a surprisingly similar peak structure as seen in the experiment [see labels (1), (2), and (3) in Figs. 5(e) and 6(e)]. In Fig. 6(e) we can again identify a frequency contribution corresponding to the area enclosed by the quantum Hall channel around the inner radius of the ring [see left vertical dashed line and label (1) in Fig. 6(e)] while the most pronounced peak is at higher frequency value, exceeding an enclosed area of πr_o^2 (see right vertical dashed line). By making use of our model system we can explain the enclosed area leading to the main peak (3) as being the sum of the two areas (1) and (2). The first area (1) corresponds to the edge channel going around the inner ring. The second area (2) originates from the motion around the charge puddle [see schematic illustrations in Figs. 6(a) and 6(c)]. Notably, the second contribution [see also labels (2) in Figs. 6(e) and 5(e)] gives rise to a higher frequency compared to the one due to the inner ring radius even though its geometrical area is smaller. This is due to the different confinement of the edge channel [see schematic illustrations in Fig. 6(a)]. While the confinement due to the graphene edges is a hard confinement with the edge modes corresponding to classical

skipping orbits, the confinement along the charge puddle is a soft confinement corresponding to a cycloid motion [full cyclotron orbits that are drifting as shown by the inset in Fig. 6(a)]. In a semiclassical description, the cycloid motion encloses a much larger area than the area enclosed by the guiding center. In particular, in a simplified model of the electron drift, the charge puddle has a different but constant filling factor and half of each cyclotron orbit is on either side of the interface. A single cyclotron orbit encloses an area of $A_C = \pi r_C^2$. The drift Δl is given by twice the difference of the cyclotron radius, i.e., $\Delta l = 2\Delta r_C \approx r_C \Delta n/n$, where n is the charge carrier density and Δn the difference in carrier densities of the bulk and the charge puddle. Thus, the electron motion encloses the effective area $A_{\mathrm{eff}} = A_C L/\Delta l = \pi L r_C n/\Delta n$ due to the cyclotron motion, where L is the length of the quantum Hall edge channel, additional to the geometric area of the charge puddle enclosed by the guiding center. In the present case, A_{eff} even dominates over the geometric size of the charge puddle resulting in the surprising effect that the peak (2) is due to the (small) charge puddle whereas (1) is due to the (large) inner radius of the ring. We have numerically checked that the dominant Aharonov-Bohm frequency of the charge puddle

alone without the inner ring is 400 1/T which corresponds to the peak (2). Including the effect of the inner ring, the dominant contribution (3) is due to electrons encircling both the charge puddle and the inner ring. However, due to a finite tunnel coupling τ [see illustrations in Figs. 6(a) and 6(c)] along the charge puddle and the boundary of the inner ring, also the fundamental frequencies (1) and (2) contribute slightly to the Fourier transform. The differences in peak positions between experiment and simulation arise from the strong dependency of the position of peak (2) from puddle diameter d_P, charge carrier density n, and density offset Δn. These quantities cannot be extracted directly from the measurements and thus only qualitative agreement is achieved. Interestingly, by having a closer look at the corresponding peaks in the FFT spectrum [see inset in Fig. 6(e)] we observe a double-peak structure (see arrows therein). This peak "splitting" is due to the valley degeneracy lifting of the edge modes and is also well observed in the calculated density of state map shown in Fig. 6(b). See in particular the white double-ring structure around the charge puddle [compare Figs. 6(a)–6(c)]. Valley degeneracy lifting is not observed in the experiment due to edge roughness, finite disorder potential, and nonzero temperature.

The visibility of all these effects in the simulation depends heavily on the specific magnetic field range, charge carrier density, puddle size, and offset in Fermi energy. However, they can be adjusted for all cases in order to observe the enhanced visibility. Since some of these parameters are unalterable in the measured sample, the rare observation of this effect becomes fairly reasonable.

IV. CONCLUSION AND SUMMARY

In conclusion, we report on the fabrication and characterization of graphene rings encapsulated in hexagonal boron nitride. We demonstrate high carrier mobilities and show magnetotransport measurements exhibiting fully phase-coherent transport. In particular, we observe the fundamental mode (h/e) and higher modes ($h/2e$ and $h/3e$) of Aharonov-Bohm conduction oscillations. In the intermediate B-field regime, we identify signatures in the magnetoconductance resulting from electron guiding and magnetic focusing of charge carriers indicating quasiballistic transport. These experimental observations are reproduced by tight-binding simulations verifying quasiballistic transport and magnetic focusing. Finally, we discuss the observation of AB oscillation in the quantum Hall regime, where at the crossover from adjacent filling factors AB oscillations with a visibility on the order of 0.7% are measured. By a detailed analysis we can attribute these oscillations to the sum of the areas enclosed by edge channels along the inner ring radius and a charge puddle connecting the inner and outer ring edge. Interestingly, the corresponding interference path, i.e., the edge mode, propagates along segments of hard- as well as soft-wall confinement.

Overall our work shows that graphene-hBN sandwiches serve as an interesting host material for studying mesoscopic physics. In particular, in view of the high tunability of the Fermi wavelength graphene may open very interesting avenues for investigating more complex interferometers, quantum billiards, Andreev billiards with hard-wall confinement, and Dirac fermion optic devices.

APPENDIX: COMPARISON TO NUMERICS

1. Implementation

The quantum transport simulation has been performed using a tight-binding approximation on a hexagonal lattice using the Kwant package [35]. We have simulated a scaled version of the graphene lattice with a lattice constant that is a factor 10 larger than the experimental situation. For ease of comparison, all the results are presented in the original units; in particular, the graphene sheet is described by its Fermi velocity $v_F = 1.15 \times 10^6$ m/s and the electron density n implemented via the Fermi energy $E_F = \hbar v_F \sqrt{\pi n}$ measured with respect to the Dirac point. We have simulated a ring with inner radius of size $r_i = 400$ nm and outer radius $r_o = 800$ nm contacted by two leads of width $w = 400$ nm as illustrated in Fig. 7(a). Following Ref. [52], we have implemented the leads by infinitely extended waveguides of highly doped graphene. The leads are connected to the device by an impedance matching zone of length 200 nm where the Fermi energy is continuously reduced from the large value in the leads to the value E_F in the device. In total, our simulation involves 7×10^5 lattice sites.

2. Conductance steps and magnetic focusing

We present the conductance of the system as a function of the homogeneous magnetic field B and the Fermi energy E_F in Fig. 7(a). We observe multiple lines of local minima in this plot. In order to investigate their origin, we have replotted the data again in Fig. 7(b) with a different axis. On one axis, we have placed a semiclassical approximation for the number of modes in a graphene ribbon of the width w of the lead that connects to the ring (also equal to the width of the ring $w = r_o - r_i$). The number of modes N is evaluated as a function of the two geometric scales in the setup, the magnetic length $l_B^2 = \hbar/eB$ and the Fermi wave number $k_F = E_F/(\hbar v_F)$, and is given by

$$N = \frac{k_F^2 l_B^2}{\pi} \arcsin\left(\frac{w}{2k_F l_B^2}\right) + \frac{w}{4\pi}\left(4k_F^2 - \frac{w^2}{l_B^4}\right)^{1/2}. \quad (A1)$$

The expression is obtained using the translational symmetry of the problem to reduce it to one dimension and then using WKB for an approximate solution [53]. On the other axis we have used the inverse cyclotron radius $r_C^{-1} = v_F eB/E_F$ in units of the inverse width w^{-1} of the geometry.

With the new axes, there are horizontal lines as well as vertical dips visible. We attribute the horizontal features to conductance quantization as they occur where the appearance of a new mode is expected in a plain graphene ribbon. The
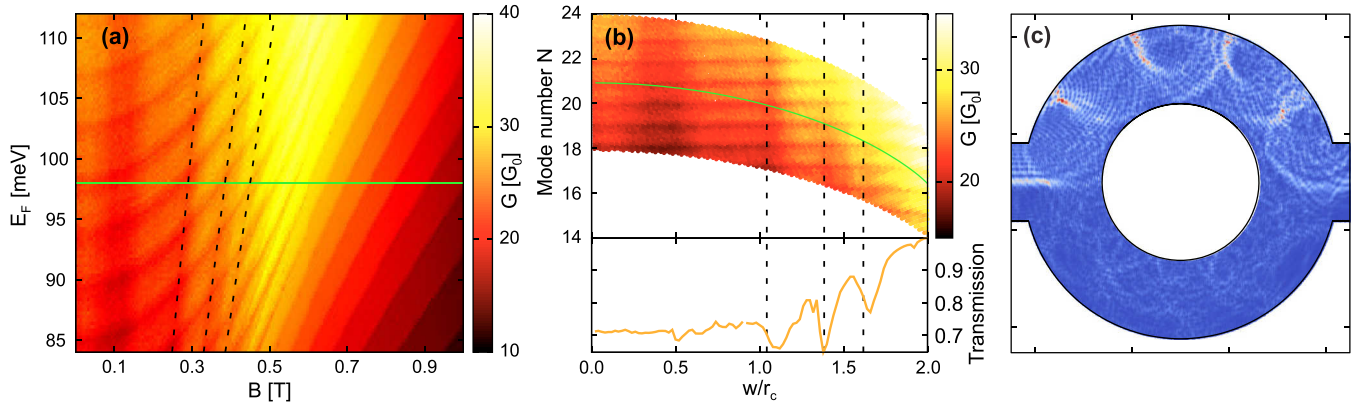
FIG. 7. (a) Conductance in units of $G_0 = 2e^2/h$ as a function of the magnetic field B and the chemical potential (Fermi energy) E_F obtained by a tight-binding calculation of a graphene ring with inner radius $r_i = 400$ nm and outer radius $r_o = 800$ nm. Indicated with dashed lines are lines of fixed cyclotron radius $r_C = 429$ nm, 569 nm, 665 nm. (b) Conductance data of (a) replotted as a function of the number of modes N propagating in the ring (of width $w = 400$ nm; see text) and the inverse cyclotron radius $1/r_C = v_F eB/E_F$ in units of the inverse width of the ring $1/w$. Minima and maxima of the conductance are approximately horizontal and vertical on this plot. The solid green line is the line of constant energy along which Fig. 8(c) is evaluated. The lower panel shows the semiclassically calculated transmission through the ring (for more details see text). (c) Plot of the density of states of an almost perfectly transmitting mode. We observe that the trajectory of the electron starting in the left lead performs a skipping orbit which after four reflections at the boundary enters the right lead.

vertical features are more intriguing and are the main focus of this section. They occur at a fixed ratios of the cyclotron orbit r_C with respect to the geometry of the ring. Therefore, it seems likely that they are connected to magnetic focusing due to the bending of the classical trajectories of the electrons in a magnetic field [54].

In order to test this hypothesis, we have performed a set of classical simulations of the transport through the ring. We have traced the path of individual trajectories propagating through the geometry assuming specular reflection at the boundary, with each trajectory starting from a random initial condition in the lead that is propagating toward the ring. We evaluated in a Monte Carlo scheme the fraction T of trajectories that propagate through the ring. In order to compare the findings with the quantum results we evaluated $G_{classic} = TNG_0$, with N being the semiclassical number of modes as in Eq. (A1).

Comparing the position of the vertical dips with the dips in the transmission probability T in Fig. 7(b), we observe a correspondence for $w \gtrsim r_C$. Note that when keeping the Fermi energy constant, we follow a bent curve (e.g., the solid green line for $E_F = 98$ meV) and thus in traces we can see both the horizontal as well as the vertical features.

Figure 7(c) displays the electron density of a specific mode that is incoming from the left lead. The maximum of the density follows semicircular paths that correspond to classical cyclotron orbits. The ratio of the cyclotron radius to the dimension of the geometry is chosen such that after four (almost specular) reflections at the upper part of the outer radius, the electron enters the right lead. Such a mode contributes to transport with a conductance close to the maximal value G_0. Increasing the magnetic field slightly decreases the cyclotron radius such that at some point there will be a reflection right before entering the right lead, with the trajectory of the electron subsequently skipping over the right lead. Here, the probability for entering the right lead is heavily lowered which results in a reduction of the conductance. As a

result the conductance oscillates as a function of the magnetic field. This is the reason for the magnetic focusing shown in Fig. 7(c).

In Fig. 8(a), we have performed a more detailed comparison for a simpler setup of a graphene disk with $r_i = 0$. The idea is that the inner radius is not important at all for the occurrence of the effect. In particular, no well-defined trajectories
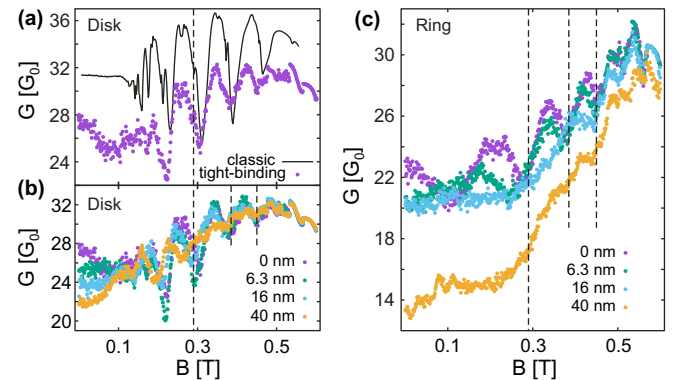

FIG. 8. (a) A comparison of the tight-binding result for the transmission to a simple classical description at a Fermi energy $E_F = 98$ meV for the transport through a disk ($r_i = 0$). A correspondence of the features in the two calculations is visible all the way up to the quantum Hall limit $w = 2r_C$. Note that the results also approximately match the results of Fig. 7(b) for $w \gtrsim r_C$ indicating that the inner radius has only an effect for small cyclotron radii. (b) Simulation of the disk geometry with a sinusoidal modulation of the outer radius with amplitude $\delta r = 0$, 6.3, 16, and 40 nm. The conductance for the disk is shown for different strength of edge roughness with the result that the position of the conductance minima are rather robust to edge roughness. (c) Finally, we also include edge roughness in the simulation of the graphene ring. We observe that with increasing edge roughness the features of quantization and magnetic focusing weaken until they resemble a shoulder-like structure that was observed in the experiments.

imposed by the constriction are required as in the case for Aharonov-Bohm oscillations. The results of the simulation are in good agreement. In particular, the classical prediction for the transmission probability T matches the results from the tight-binding calculation rather well up to the value $w = 2r_C$ where the quantum Hall effect evolves. For small cyclotron radii with $w \gtrsim r_C$ there is essentially no difference between ring and disk geometry since the number of trajectories touching the inner boundary gets significantly reduced.

The conductance oscillations due to the magnetic focusing are easily distinguishable from universal conductance fluctuations. The magnitude is larger than a conductance quantum as multiple modes simultaneously fulfill the focusing condition. The effect is only dependent on the cyclotron radius and the device geometry. For an estimation of the thermal stability, we compare the magnitude of the thermal fluctuations of the cyclotron radius $\Delta r_C \approx k_B T / v_F e B$ with the width of the ring arm w. For the experimental parameters ($B = 1$ T and $T \leqslant 4.2$ K), we obtain the estimate $\Delta r_C \approx 0.4$ nm which is orders of magnitude smaller than w.

3. Edge roughness

After modeling the basics of magnetic focusing, we concentrate now on the extension of the simulation for a better agreement with the experimental findings. In the experiment no quantized conductance is observed (horizontal features) and the oscillations due to magnetic focusing appear as plateaus in the magnetoconductance [compare Fig. 4(e)]. Differently from the experimental situation, we have considered a perfect

graphene ring without any disorder and edge roughness so far. From the large mobility measured in the system, we conclude that impurity scattering is negligible in the bulk of the device. Therefore, we attribute the difference between the experimental data and the simulation to edge roughness at the graphene boundaries. For a simple model of edge roughness, we modulate the radius of the outer ring $r_o(\theta) = r_o + \delta r \cos(n\theta)$ with $n = 20$ and variable amplitude δr [55]. Note that we do not intend to realistically model the edge roughness of the experimental situation. One of the reasons is that the chemistry at the edge is not sufficiently understood. But even more importantly, as we simulate a scaled version of the graphene lattice, edge defects that appear on the scale of single atoms cannot be included even in principle. As a result, we model the edge roughness by a single effective parameter δr in the simple model given above. Figure 8(b) shows the effect of the edge roughness on the magnetic focusing in the disk geometry. As it is evident from the plot, the features due to magnetic focusing are rather robust toward the inclusion of edge roughness.

Figure 8(c) makes the connection to the experiment as it displays the situation of a graphene ring with the effect of edge roughness taken into account. We see that increasing the edge roughness from $\delta r = 0$ to $\delta r = 6.3$ nm starts suppressing the features of quantization and magnetic focusing. At an edge roughness of about $\delta r = 16$ nm the features are transformed to a more shoulder-like behavior (e.g., between the two vertical dashed lines). The experimental situation is best described with this level of edge disorder [56].

---

[1] See, e.g., Y. Imry, *Introduction to Mesoscopic Physics* (Oxford University Press, New York, 2002).

[2] P. A. Lee and A. D. Stone, Phys. Rev. Lett. **55**, 1622 (1985).

[3] B. J. van Wees, H. van Houten, C. W. J. Beenakker, J. G. Williamson, L. P. Kouwenhoven, D. van der Marel, and C. T. Foxon, Phys. Rev. Lett. **60**, 848 (1988).

[4] A. C. Bleszynski-Jayich, W. E. Shanks, B. Peaudecerf, E. Ginossar, F. von Oppen, L. Glazman, and J. G. E. Harris, Science **326**, 272 (2009).

[5] R. A. Webb, S. Washburn, C. P. Umbach, and R. B. Laibowitz, Phys. Rev. Lett. **54**, 2696 (1985).

[6] A. K. Geimand and I. V. Grigorieva, Nature (London) **499**, 419 (2013).

[7] L. Banszerus, M. Schmitz, S. Engels, M. Goldsche, K. Watanabe, T. Taniguchi, B. Beschoten, and C. Stampfer, Nano Lett. **16**, 1387 (2016).

[8] P. Boggild, J. M. Caridad, C. Stampfer, G. Calogero, N. R. Papior, and M. Brandbyge, Nat. Commun. **8**, 15783 (2017).

[9] For a review, see N. Agrawal, S. Ghosh, and M. Sharma, Int. J. Mod. Phys. B **27**, 1341003 (2013).

[10] A. F. Young and P. Kim, Nat. Phys. **5**, 222 (2009).

[11] C. Handschin, P. Makk, P. Rickhaus, M.-H. Liu, K. Watanabe, T. Taniguchi, K. Richter, and C. Schönenberger, Nano Lett. **17**, 328 (2017).

[12] T. Taychatanapat, K. Watanabe, T. Taniguchi, and P. Jarillo-Herrero, Nat. Phys. **9**, 225 (2013).

[13] G.-H. Lee, G.-H. Park, and H.-J. Lee, Nat. Phys. **11**, 925 (2015).

[14] Q. Wilmart, S. Berrada, D. Torrin, V. H. Nguyen, G. Fève, J.-M. Berroir, P. Dollfus, and B. Plaçais, 2D Mater. **1**, 011006 (2014).

[15] I. V. Borzenets, F. Amet, C. T. Ke, A. W. Draelos, M. T. Wei, A. Seredinski, K. Watanabe, T. Taniguchi, Y. Bomze, M. Yamamoto, S. Tarucha, and G. Finkelstein, Phys. Rev. Lett. **117**, 237002 (2016).

[16] Y. Aharonov and D. Bohm, Phys. Rev. **115**, 485 (1959).

[17] G. Timp, A. M. Chang, J. E. Cunningham, T. Y. Chang, P. Mankiewich, R. Behringer, and R. E. Howard, Phys. Rev. Lett. **58**, 2814 (1987).

[18] S. Russo, J. B. Oostinga, D. Wehenkel, H. B. Heersche, S. S. Sobhani, L. M. K. Vandersypen, and A. F. Morpurgo, Phys. Rev. B **77**, 085413 (2008).

[19] M. Huefner, F. Molitor, A. Jacobsen, A. Pioda, C. Stampfer, K. Ensslin, and T. Ihn, Phys. Status Solidi B **246**, 2756 (2009).

[20] M. Huefner, F. Molitor, A. Jacobsen, A. Pioda, C. Stampfer, K. Ensslin, and T. Ihn, New J. Phys. **12**, 043054 (2010).

[21] D. Smirnov, H. Schmidt, and R. J. Haug, Appl. Phys. Lett. **100**, 203114 (2012).

[22] D. Cabosart, S. Faniel, F. Martins, B. Brun, A. Felten, V. Bayot, and B. Hackens, Phys. Rev. B **90**, 205433 (2014).

[23] J. Schelter, D. Bohr, and B. Trauzettel, Phys. Rev. B **81**, 195441 (2010).

[24] J. Schelter, P. Recher, and B. Trauzettel, Solid State Commun. **152**, 1411 (2012).

[25] A. Mreńca-Kolasińska, S. Heun, and B. Szafran, Phys. Rev. B **93**, 125411 (2016).

[26] C. Stampfer, J. Güttinger, S. Hellmüller, F. Molitor, K. Ensslin, and T. Ihn, Phys. Rev. Lett. **102**, 056403 (2009).

[27] P. Gallagher, K. Todd, and D. Goldhaber-Gordon, Phys. Rev. B **81**, 115409 (2010).

[28] C. R. Dean, A. F. Young, I. Meric, C. Lee, L. Wang, S. Sorgenfrei, K. Watanabe, T. Taniguchi, P. Kim, K. L. Shepard, and J. Hone, Nat. Nanotechnol. **5**, 722 (2010).

[29] A. S. Mayorov, R. V. Gorbachev, S. V. Morozov, L. Britnell, R. Jalil, L. A. Ponomarenko, P. Blake, K. S. Novoselov, K. Watanabe, T. Taniguchi, and A. K. Geim, Nano Lett. **11**, 2396 (2011).

[30] L. A. Ponomarenko, A. K. Geim, A. A. Zhukov, R. Jalil, S. V. Morozov, K. S. Novoselov, I. V. Grigorieva, E. H. Hill, V. V. Cheianov, V. I. Falko, K. Watanabe, T. Taniguchiand, and R. V. Gorbachev, Nat. Phys. **7**, 958 (2011).

[31] L. Wang, I. Meric, P. Y. Huang, Q. Gao, Y. Gao, H. Tran, T. Taniguchi, K. Watanabe, L. M. Campos, D. A. Muller, J. Guo, P. Kim, J. Hone, K. L. Shepard, and C. R. Dean, Science **342**, 614 (2013).

[32] B. Terrés, L. A. Chizhova, F. Libisch, J. Peiro, D. Jörger, S. Engels, A. Girschik, K. Watanabe, T. Taniguchi, S. V. Rotkin, J. Burgdörfer, and C. Stampfer, Nat. Commun. **7**, 11528 (2016).

[33] S. Engels, A. Epping, C. Volk, S. Korte, B. Voigtländer, K. Watanabe, T. Taniguchi, S. Trellenkamp, and C. Stampfer, Appl. Phys. Lett. **103**, 073113 (2013).

[34] D. Bischoff, A. Varlet, P. Simonet, M. Eich, H. C. Overweg, T. Ihn, and K. Ensslin, Appl. Phys. Rev. **2**, 031301 (2015).

[35] C. Groth, M. Wimmer, A. Akhmerov, and X. Waintal, New J. Phys. **16**, 063065 (2014).

[36] From the SFM image we extract a 4W path length of $L \approx 3\ \mu$m and with accounting twice the ring width $w = 350$ nm for path width W we estimate the aspect ratio $L/W \approx 4$.

[37] The mean-free path $l_m = \hbar\mu\sqrt{\pi\alpha|V_G - V_{CNP}|}$ is calculated as a lower and an upper estimate for $|V_G - V_{CNP}| = 5$–30 V and $\mu = 60\,000$–$100\,000$ cm^2/V s.

[38] For more details, see N. J. G. Couto, D. Costanzo, S. Engels, D.-K. Ki, K. Watanabe, T. Taniguchi, C. Stampfer, F. Guinea, and A. F. Morpurgo, Phys. Rev. X **4**, 041019 (2014).

[39] D. A. Abanin and L. S. Levitov, Phys. Rev. B **78**, 035416 (2008).

[40] The periodicity of AB oscillations can be determined by the sample geometry $\Delta B_{AB} = h/e\pi r^2$, where the radius r is set to $r_i = 405$ nm, $\bar{r} = 580$ nm, and $r_o = 755$ nm, respectively.

[41] We define visibility as the ratio of AB amplitude and the 2W conductance at zero magnetic field $\Delta G_{AB}/G_{2W}(B = 0)$.

[42] P. Vasilopoulos, O. Kálmán, F. M. Peeters, and M. G. Benedict, Phys. Rev. B **75**, 035304 (2007).

[43] C. J. B. Ford, T. J. Thornton, R. Newbury, M. Pepper, H. Ahmed, D. C. Peacock, D. A. Ritchie, J. E. F. Frost, and G. A. C. Jones, Appl. Phys. Lett. **54**, 21 (1988).

[44] A. E. Hansen, A. Kristensen, S. Pedersen, C. B. Sorensen, and P. E. Lindelof, Phys. Rev. B **64**, 045327 (2001).

[45] B. Grbic, R. Leturcq, T. Ihn, K. Ensslin, D. Reuter, and A. D. Wieck, Phys. Rev. Lett. **99**, 176803 (2007).

[46] L. C. Mur, C. J. P. M. Harmans, and W. G. van der Wiel, New J. Phys. **10**, 073031 (2008).

[47] C. W. J. Beenakker and H. van Houten, in *Solid State Physics*, edited by H. Ehrenreich and D. Turnbull (Academic, New York, 1991).

[48] D.-K. Ki and A. F. Morpurgo, Phys. Rev. Lett. **108**, 266601 (2012).

[49] J. Martin, N. Akerman, G. Ulbricht, T. Lohmann, J. H. Smet, K. von Klitzing, and A. Yacoby, Nat. Phys. **4**, 144 (2007).

[50] J. Xue, J. Sanchez-Yamagishi, D. Bulmash, P. Jacquod, A. Deshpande, K. Watanabe, T. Taniguchi, P. Jarillo-Herrero, and B. J. LeRoy, Nat. Mater. **10**, 282 (2011).

[51] Forschungszentrum Jülich, GmbH, HNF–Helmholtz Nano Facility, Journal of Large-Scale Research Facilities **3**, A112 (2017).

[52] J. Wurm, M. Wimmer, H. U. Baranger, and K. Richter, Semicond. Sci. Technol. **25**, 034003 (2010).

[53] G. Montambaux, Eur. Phys. J. B **79**, 215 (2011).

[54] H. van Houten and C. W. J. Beenakker, Quantum point contacts and coherent electron focusing, in *Analogies in Optics and Micro Electronics*, edited by W. van Haeringen and D. Lenstra (Kluwer, Dordrecht, 1990).

[55] We only include edge roughness of the outer edge as the physics is dominated by this edge. We have checked that edge roughness on the inner edge has a negligible impact on the final results.

[56] Moreover, we observe that the shoulder-like curve even turns on a rather monotonic behavior at higher strength of the edge disorder.